

Picosecond view of a martensitic transition and nucleation in the shape memory alloy $\text{Mn}_{50}\text{Ni}_{40}\text{Sn}_{10}$ by four-dimensional transmission electron microscopy

Ming Zhang,^{1,2} Gaolong Cao,^{1,2} Huanfang Tian,^{1,*} Shuaishuai Sun,¹ Zhongwen Li,¹ Xingyuan Li,¹ Cong Guo,¹ Zian Li,¹ Huaixin Yang,^{1,2} and Jianqi Li^{1,2,3,†}

¹*Beijing National Laboratory for Condensed Matter Physics, Institute of Physics, Chinese Academy of Sciences, Beijing 100190, China*

²*School of Physical Sciences, University of Chinese Academy of Sciences*

³*Collaborative Innovation Center of Quantum Matter, Beijing 100190, China*

(Received 11 April 2017; revised manuscript received 24 October 2017; published 6 November 2017)

The photoinduced martensitic (MT) transition and reverse transition in a shape memory alloy $\text{Mn}_{50}\text{Ni}_{40}\text{Sn}_{10}$ have been examined by using high spatiotemporal resolution four-dimensional transmission electron microscopy (4D-TEM), and the experimental results clearly demonstrate that the MT transition and reverse transition in this Heusler alloy contain a variety of structural dynamic features at picosecond time scales. The 4D-TEM imaging and diffraction observations clearly show that MT transition and MT domain nucleation, which are related to cooperative atomic motions, occur at between 10 and 20 ps, depending on the thickness of the sample. Moreover, a strong coupling between the MT transition and lattice breathing mode is discovered in this system, which can result in a periodic structural oscillation between the MT phase and austenitic (AUS) phase. This allows us to directly observe the MT nucleation and domain wall motions in transient states using high spatiotemporal imaging. A careful analysis of the ultrafast images demonstrates the presence of remarkable transient states, which exhibit the essential features of MT nucleation, lattice symmetry breaking, and a rapid growth of MT plates. These results not only provide insights into the time-resolved structural dynamics and elementary mechanisms that govern the MT transition but also contribute to the development of a novel technique for future 4D-TEM investigations.

DOI: [10.1103/PhysRevB.96.174203](https://doi.org/10.1103/PhysRevB.96.174203)

Over the past decades, significant progress has been made in the study of structural and physical properties of Heusler alloys, which are considered as important functional materials from both the academic and technological perspectives [1]. For instance, the large magnetically induced strain and magnetocaloric effects in NiMnGa [2,3] and NiMnSn [4,5] have been extensively investigated based on the interplay among ferromagnetism, martensitic (MT) phase transition, and notable thermodynamic properties. In particular, this type of shape memory alloy has been widely exploited in a range of applications including automotive, aerospace, robotic, biomedical, and microelectromechanical systems [6,7]. It is well known that the martensitic transformation as a typical diffusionless transformation exhibits a variety of collective phenomena involving the synchronous movements of atoms [8]. Despite the fact that detailed structural characterization of both AUS and MT phases has been achieved using static characterization tools, experimentally direct imaging of the dynamics of MT phase transition remains a significant challenge.

Recently, ultrafast electron diffraction [9–11], ultrafast x-ray diffraction [12–14], and four-dimensional ultrafast transmission electron microscopy (4D-UTEM) [15–18] have been demonstrated as effective techniques for revealing the remarkable ultrafast structural dynamic features and structural phase transitions in a variety of materials, such as nanotubes [19,20], charge density waves (CDWs) [21,22], and biomaterials [23,24]. 4D-TEM is a novel technique for real-space imaging and reciprocal-space diffraction; it is capable of revealing the essential transient states in phase transitions and

can potentially be a significant technique for characterizing MT materials. $\text{Mn}_{50}\text{Ni}_{40}\text{Sn}_{10}$ is the classical Heusler magnetic shape memory alloy with a magnetic transition at $T_c = 270$ K and a MT transition at $T_m = 214$ K [4] (from the high-temperature cubic AUS phase to the orthorhombic MT phase). This Heusler alloy contains visible MT domains at low temperature, and upon ultrafast photoexcitation, it undergoes a dynamic evolution from the MT phase to the high-temperature AUS phase, which is associated with collective microstructure changes.

In this paper, we report our study of the MT phase transition and reverse transition in $\text{Mn}_{50}\text{Ni}_{40}\text{Sn}_{10}$, as observed using high spatiotemporal resolution 4D-TEM [19]. We demonstrate that the MT phase transition occurs at a picosecond scale, and a coherent coupling between photoexcitation and structural transformation is observed for the acoustic breathing mode [25], which strongly modulated the MT transition and domain nucleation. The transient states and relevant dynamical structures have also been extensively analyzed.

Figure 1 shows the fundamental structural features and microstructural changes pertaining to static AUS and MT phases. It is observed that visible structural domains arise from the structural transition from the high-temperature cubic AUS phase to the orthorhombic MT phase. Additionally, a structural modulation (i.e., a 5 M superstructure) along the [100] zone-axis direction in the MT phase is believed to be critical for structural stability, based on theoretical calculations for a particular minimum in the thermodynamic free energy [26]. Due to the collective atomic motion during the MT transition, a large strain/stress commonly appears at the domain walls, which can result in measurable features in the diffraction-contrast images [27]. We used an objective aperture to form image contrasts with clear structural domains and

*hftian@iphy.ac.cn

†ljq@iphy.ac.cn

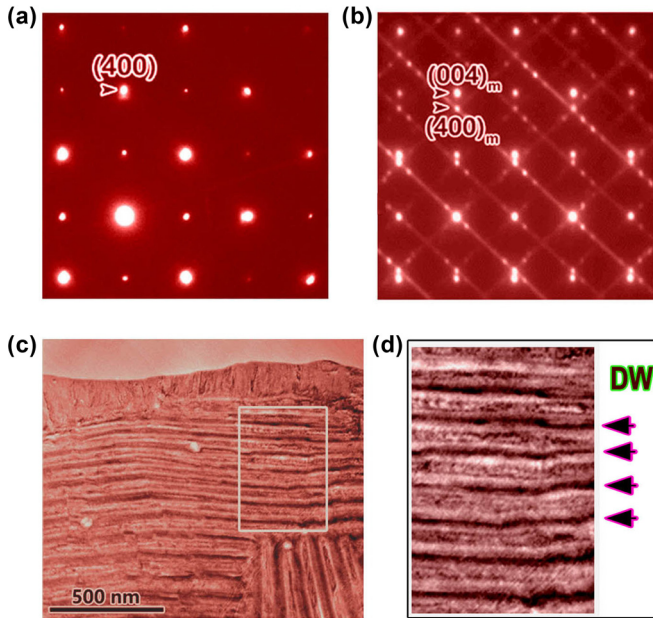


FIG. 1. Selected-area electron diffraction (SAED) patterns and bright-field images of $\text{Mn}_{50}\text{Ni}_{40}\text{Sn}_{10}$. (a) SAED pattern of the AUS phase taken along the $[001]$ zone-axis direction at room temperature. (b) SAED pattern of the MT phase at 100 K, illustrating the presence of spot splitting and the 5M superstructure. (c) Bright-field TEM image of the MT phase, which shows the domain lamella in the a - b plane. (d) Enlarged image of the area indicated by the white rectangle in (c); the arrows show domain walls.

found the contrast alteration (e.g., the relatively dark contrast in some areas) is related to the diffraction effects arising from the interplay among the 5M superstructure, MT variants, and local structural distortion, as clearly indicated in Fig. 1(d). These visible contrast changes in the 4D-TEM images allow us to directly observe the transient states through the phase transition and, in particular, the nucleation and growth of the MT domain/walls in $\text{Mn}_{50}\text{Ni}_{40}\text{Sn}_{10}$, as discussed below.

To directly observe the ultrafast changes of the microstructure and relevant transient states at the MT transition of $\text{Mn}_{50}\text{Ni}_{40}\text{Sn}_{10}$, we first prepared the specimen in martensitic state at 100 K using a liquid-nitrogen cooling TEM holder and then carried out laser-pump electron-probe experiments (schematics in Fig. S1 in Supplemental Material [28]). It is clearly demonstrated that the $\text{Mn}_{50}\text{Ni}_{40}\text{Sn}_{10}$ sample undergoes a MT transition at low temperature, and the MT phase has an orthorhombic structure with complex modulated microstructural features, as shown in Fig. 1. The size of the MT domains generally ranges from 20 to 100 nm. Moreover, the 5M-superstructure modulations often appear within the MT domains [4,27]. Our 4D-TEM observations reveal that through the MT transition, alterations of the MT domain structures, as well as the strain/stress at domain walls, can result in measurable contrast changes in both the bright-field and dark-field images. A clear ultrafast lattice motion associated with MT transition is observed at the picosecond scale. Figure 2(a) shows three typical 4D-TEM images obtained at time delays of $t = -20, 0,$ and 20 ps (negative time delay means images taken by pulse electrons before the arrival of pump-pulse

laser). These images were all taken from a $\text{Mn}_{50}\text{Ni}_{40}\text{Sn}_{10}$ crystal, which primarily exhibits clear MT stripe domains at 100 K, as observed along the $[110]$ direction and discussed in previous *in situ* TEM investigations [4]. The pumping laser in this case has a beam diameter of $60 \mu\text{m}$ on a specimen with a laser fluence of 5 mJ cm^{-2} . The temperature rise by a single laser pulse is estimated to be about 150 K using the formula $\Delta T = [F(1 - e^{-\alpha t})]/c\rho t$, with parameters of laser-pumping fluence F , linear absorption coefficients α on the order of $1/100 \text{ nm}^{-1}$, thickness t , specific heat c , and density of the specimen ρ . To analyze the transient states that appear during the MT transition, contrast profiles from the selected area [green rectangle marked in Fig. 2(a)] are presented in Fig. 2(b). These profiles illustrate the fundamental domain features from images recorded in consecutive time scans, which are associated with an ultrafast annihilation of the MT lamella upon pulsed-laser excitations. To obtain the systematic dynamic data for analyzing this transition, we have also examined several $\text{Mn}_{50}\text{Ni}_{40}\text{Sn}_{10}$ crystals with different thicknesses ranging from 40 to 100 nm. We found that the photoinduced MT transition can be approximately fitted using an exponential function to yield a time constant of about 16 ps.

It should be noted that the photoinduced transition of MT domains strongly depends on the sample thickness. Moreover, the movements of domain walls can be frequently observed throughout the photoinduced transition, as indicated by the short lines on each peak in Fig. 2(b), and the relative intensity of the domains (or domain walls) rapidly changes between 0 and 10 ps, as observed in the peak-intensity distribution at the line-scan profiles. Figure 2(c) shows the time dependences of the domain intensities obtained from areas of *A* and *B* marked in Fig. 2(a). It is estimated that area *A* has a larger thickness (~ 50 nm) than does area *B* (~ 30 nm). Importantly, the MT transition and the transient states are essentially driven by cooperative atomic motions, and our 4D-TEM observations suggest that the remarkable changes of the domain structure due to the atomic motions and structural transition mainly occur between 5 and 15 ps (see Movie S1 of Supplemental Material [28]), which demonstrates the occurrence of a dynamical MT to AUS phase transformation. The changes in the bright-field TEM images are essentially correlated with the changes to the electron diffractions for specific domains (or walls), (i.e., the diffraction contrast image). Therefore, the disappearance of MT domains associated with the phase transition can be quantitatively fitted by an exponential function $I(t) = I_0[1 - \exp(-t/\tau)]$, and the time constants are estimated to be 10 ps for area *B*, which has a thin area, and 22 ps for the relatively thicker area *A*.

This difference is believed to arise from the deposited energy density and the strains/stress relaxation [29–31]. According to the Beer-Lambert law (Fig. S6 in Supplemental Material [28]), the deposited energy density and the temperature rise, following pulsed-laser excitation, can decrease in the relatively thicker areas, which can slow down the atomic motions after the structural transition. In addition to the bright-field images, the corresponding electron-diffraction measurements obtained through the photoinduced MT transition also reveal structural phase transition and notable lattice dynamic features. The $\text{Mn}_{50}\text{Ni}_{40}\text{Sn}_{10}$ alloy typically shows a MT structural-phase transition at approximately 214 K. As a

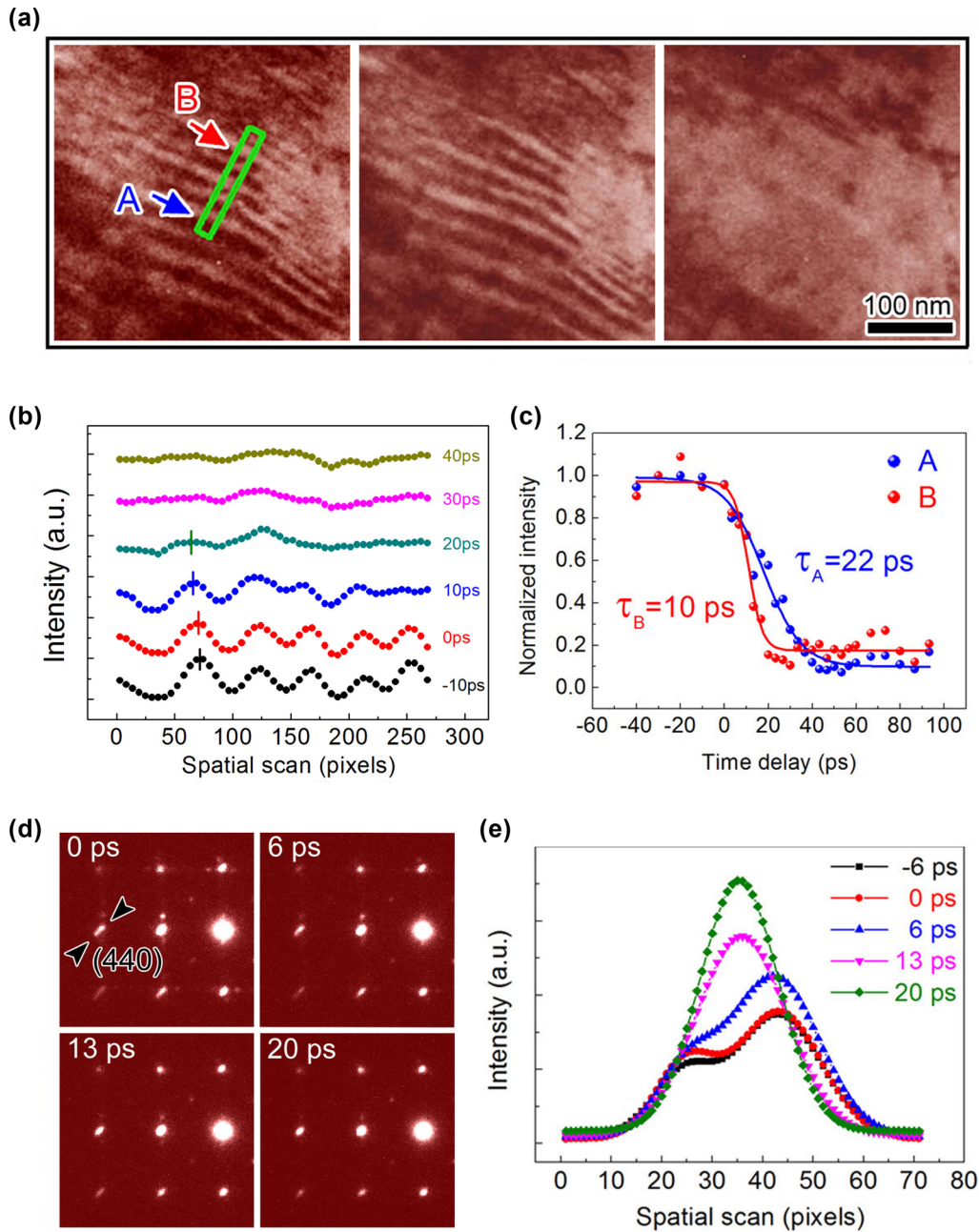


FIG. 2. Time-resolved experimental data for the photoinduced phase transition from the MT phase to AUS phase. (a) Three typical 4D-TEM images obtained at time delays of $t = -20$, 0 , and 20 ps, with a laser-pumping fluence of 5 mJ cm^{-2} . (b) Time-dependent profiles for the MT domains in the area outlined by the green rectangle in (a); the ultrafast annihilation of the MT domains is demonstrated. The short lines on each peak show the visible movements of domain walls through the MT transition. (c) Domain intensities obtained from areas *A* and *B* as a function of the time delay. The difference in their time constants is attributed to the thickness distinction between area *A* (50 nm) and area *B* (30 nm). (d) SAED patterns taken along the $[001]$ zone axis at different time delays; the arrows show visible spot splitting. (e) Ultrafast changes of the spot splitting indicated by the arrows in (d), obtained with a laser-pumping fluence of 10 mJ cm^{-2} , which demonstrate a picosecond transition from the orthorhombic MT phase to the cubic AUS phase. Spot splitting becomes almost invisible for $t > 13$ ps.

result, the low-temperature orthorhombic phase often shows clear spot splitting in the $[001]$ zone-axis electron-diffraction pattern because of the difference in the a and b lattice parameters for the MT domains. For instance, the (400) and (440) spots at $t = 0$ in Fig. 2(d) exhibit visible splitting along the $\langle 110 \rangle_{\text{orth}}$ direction, and a temporal variation of the splitting spots during 0–20 ps can be used to characterize the ultrafast lattice transition in Fig. 2(d). Figure 2(e) presents

the temporal evolution of the orthorhombic splitting distance [i.e., $2(1/d_{010} - 1/d_{100})$] changes, showing that the splitting of the diffraction spots changes quickly at 10 ps and becomes almost invisible at 13 ps. These diffraction results are in good agreement with the above 4D-TEM direct observations.

In the shape memory alloys, the application of additional stress or the presence of lattice shearing could lead to notable changes of the microstructure and often yield a

visible alteration to MT transition, as discussed extensively in Ref. [29]. In our 4D-TEM measurements, we often observe that the photoexcitation of the thin TEM specimen, in particular the round-trip breathing oscillation, could result in apparent modulations on interplanar spaces and a local structural distortion, and these structural changes could result in a periodic lattice shearing in the ultrafast transformation [25]. In previous reports, this type of structural phenomena has been observed in several materials, such as graphite [25] and aluminum crystals [9] in ultrafast electron or x-ray diffraction experiments. The fundamental mechanism responsible for generating breathing oscillation modes in $Mn_{50}Ni_{40}Sn_{10}$ materials is also discussed; i.e., the pumping laser excites a large population of valence electrons, which could shift the equilibrium positions of the

crystal lattice, causing the atoms to vibrate around the new equilibrium position [32].

We now proceed to discuss this intriguing phenomenon of periodic structural oscillation coupled with the MT transition in $Mn_{50}Ni_{40}Sn_{10}$ subsequent to photoexcitation. Figure 3(a) shows a series of ultrafast images illustrating the MT transition and microstructure changes coupled with a periodic oscillation. The stripe contrasts of MT domain structures are seen in the image taken at $t_0 = 0$ ps. After the arrival of the pumping laser pulses, the time-resolved images in Fig. 3(a) show rapid contrast changes, which reflect the fast alterations of the MT domains and microstructural features. First, it is clearly demonstrated that the annihilation of MT domains (from t_0 to t_1) at ~ 23 ps is due to the photoinduced

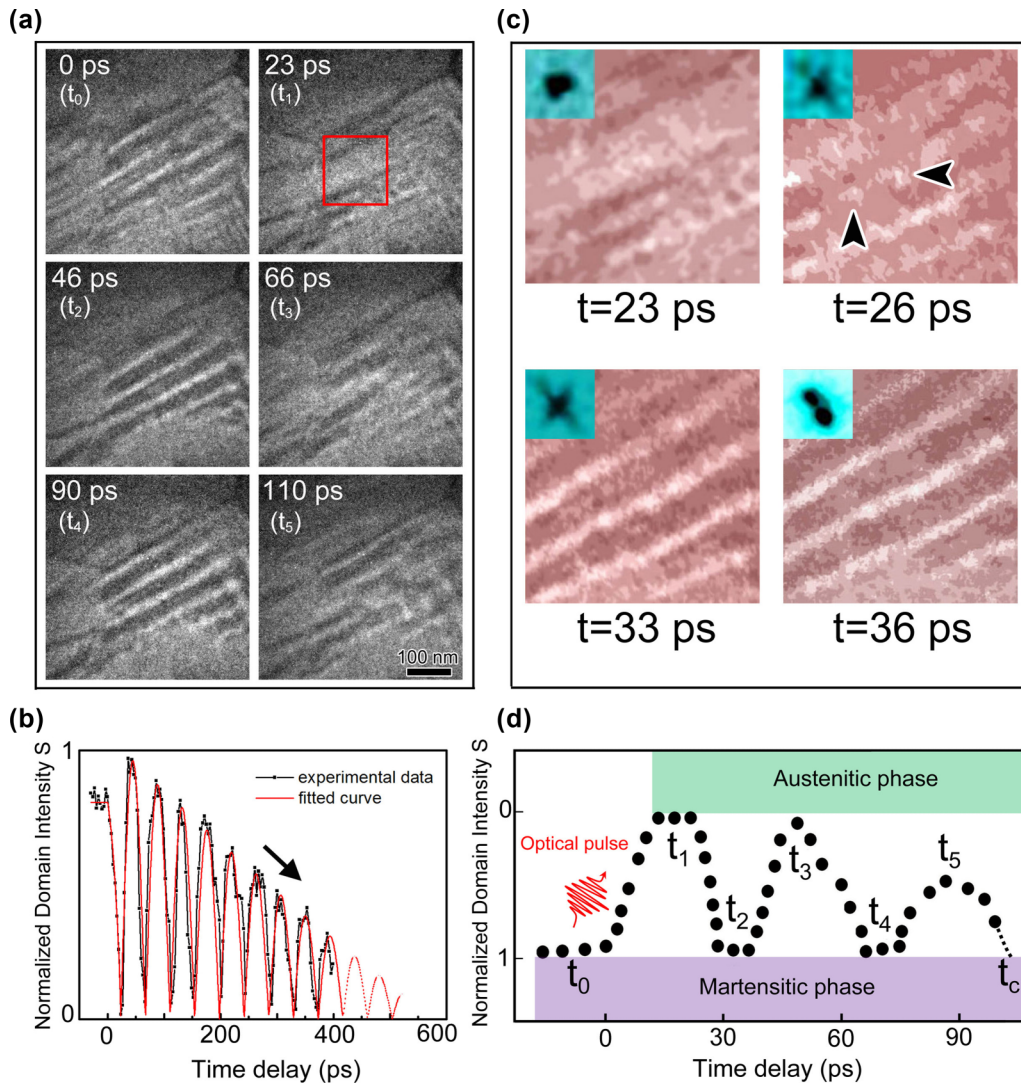


FIG. 3. 4D-TEM images taken from an area with better reversibility for analyzing MT domain nucleation. (a) Series of ultrafast micrographs showing the periodic annihilation and creation of domains with a laser-pumping fluence of 10 mJ cm^{-2} ; the thickness in this area is estimated to be approximately 80 nm, as typically illustrated in Fig. S5 of Supplemental Material [28]. (b) Structural oscillation obtained from (a) and Movie S2 of Supplemental Material [28] in which about 100 frames of dynamic images are shown; we can clearly see the relaxation time of oscillation is over 500 ps. Domain intensities S are obtained from $S = [\Sigma(X_i - X_0)/N]1/2$, as illustrated in the Method section in Supplemental Material [28]. (c) Careful analysis of the domain nucleation for the boxed area in (a) between $t = 23$ ps and $t_2 = 46$ ps; the presence of tweedlike patterns is evident. The inserted figure in each frame illustrates the progress of the (080) spots followed by MT domain nucleation. (d) Schematic illustration showing the structural oscillation of $Mn_{50}Ni_{40}Sn_{10}$ due to strong coupling between the MT transition and breathing mode.

MT to AUS phase transition, as similarly seen in Fig. 2(a). Subsequently, the breathing phonons periodically modulate the lattice structure and MT domains. For instance, from frame t_1 to t_2 , a reverse transition occurs, during which the domain wall (DW) nucleation and growth process of the structural domains finish. As previously discussed for NiMnGa [33] and graphite [25], the round-trip breathing oscillation can be examined in the diffraction measurements (reciprocal space) for the specimen that is thinner than the optical absorption length (~ 140 nm). Our observation directly reveals the pulse-laser-driven microstructural alternations in real space using the high spatiotemporal resolution 4D-TEM.

Since the $\text{Mn}_{50}\text{Ni}_{40}\text{Sn}_{10}$ specimen in our investigations is freestanding, open boundary conditions are assumed here, and the specimen thickness is extracted using the formula $L = v/2f$, where $v = 4.0$ nm/ps is the speed of sound and f is the extracted linear frequency (comparable to the speed of sound in a related system). The vibration shown in Fig. 3(b) is approximately 25 GHz, and by using the speed of sound in NiMnGa [33] the specimen thickness is estimated to be ~ 80 nm, which is in agreement with the thickness obtained from the electron-energy-loss spectroscopy (EELS) measurements [34] (Fig. S5 in Supplemental Material [28]). Moreover, the oscillations of the domain structures persist for a long time, and t_c is estimated to be longer than 500 ps, as shown in Fig. 3(b).

To obtain the relationship between the structural features and the DW nucleation of the MT domains, we have performed a careful analysis on the ultrafast images and the corresponding diffraction patterns obtained from t_1 to t_2 , as shown in Fig. 3(c) and in Movie S2 of Supplemental Material [28]. The first frame in Fig. 3(c) exhibits the bright-field image of the central area marked in Fig. 3(a) ($t_1 = 23$ ps), in which the sample adopts a cubic AUS structure. In Fig. 3(c), the presence of the visible transient strain/stress from MT nucleation exhibits tweedlike contrasts in the otherwise featureless contrasts of the AUS phase. The most remarkable structural feature observed between t_1 and t_2 is the appearance of a tweedlike transient state. It is first observed in the image taken at 26 ps, and the images then start to show fine speckled contrasts, as indicated by the arrows (i.e., DWs as small as a few nanometers). For good understanding of the lattice distortion and image contrast in this transient state, we used a structural model and relevant results in tweed structure as discussed in the Method section of Ref. [35]. Analysis of the series of ultrafast images and the diffraction patterns reveals that these microstructural features commonly occur in transient states between the MT phase and AUS phase, i.e., a typical pattern with a clear fluctuation accompanied by the DW nucleation. Moreover, the appearance of the tweedlike structure is associated with the cubic symmetry breaking, which yields nucleation of MT domains with nanometer sizes. The tweed structure can be well identified by the cross-shaped diffraction streaks accompanying the main diffraction spots, which is in contrast to the diffraction spot splitting for the MT phase: The diffraction streaks go along the [100] and [010] zone directions, as shown in the insets ($t = 26$ and 33 ps) of Fig. 3(c). Furthermore, we also observed that the transient, tweedlike structures occur in the course of breathing oscillations with relatively longer delay times, as seen in Movie S2 of Supplemental Material [28]. Analysis

of the temporal evolution of the ultrafast image contrasts and the streaking/splitting of diffraction spots reveals that the MT nucleation yields visible structural fluctuations, and the MT nuclei commonly show the coherent twinning nature along either the (110) or ($\bar{1}\bar{1}0$) planes.

Based on the 4D-TEM experimental data on a few well-characterized $\text{Mn}_{50}\text{Ni}_{40}\text{Sn}_{10}$ crystals with different sizes, we found that the frequency of the structural oscillation depended on the thickness of the specimen. The thicknesses of the specimens measured by the EELS are given in Fig. S5 of Supplemental Material [28]. The measured frequency, as discussed in a previous paper, is thus the lowest-order longitudinal acoustic phonon mode quantized by the specimen thickness L [25,36]. In our measurements on a set of well-characterized samples (see Table S1 of Supplemental Material [28]), the average period for the structural oscillations is estimated to be approximately 30 ps associated with a visible alteration of the MT domains, as shown in Fig. 3(d). It should be noted that the structure of the domains undergoes a relatively longer time oscillation and relaxation, arising from strong effects of the photoexcited lattice breathing modes.

Our analysis of ultrafast structural dynamics of a few $\text{Mn}_{50}\text{Ni}_{40}\text{Sn}_{10}$ crystals demonstrates that the breathing modes are coupled to the MT transition in $\text{Mn}_{50}\text{Ni}_{40}\text{Sn}_{10}$. Consequently, remarkable periodic modulations on the transient states occur as significant oscillations of annihilation/recreation of the MT domains in picosecond time scales. This oscillatory behavior fundamentally arises from an excitation of the lowest-order longitudinal acoustic phonons [37].

Based on these high spatiotemporal resolution observations, we now discuss the collective atomic motions and lattice symmetry breaking, as they are all clearly important for understanding the essential transient states and the mechanism for the MT transition. Although the structural defects, crystal size, and structural hysteresis could result in certain inaccuracies for identifying the lifetimes of the transient states, the fundamental structural changes correlated with MT nucleation, symmetry breaking, and lattice motions can be clearly observed for the transformation from the MT phase to AUS phase and the AUS phase to MT phase. In Fig. 4, we summarized the temporal dynamics of the MT transition in a number of $\text{Mn}_{50}\text{Ni}_{40}\text{Sn}_{10}$ crystals. In Fig. 4(a) of transient 1, the nucleation of the MT phase is found to follow the twinning mechanism. In addition to the visible structural fluctuations of the MT nuclei, their growth orientations are notably associated with the tetragonal symmetry of the cubic AUS phase. Therefore, the twinning planes are located on two crystallographically equal planes [i.e., the (110) and ($\bar{1}\bar{1}0$) planes]. The critical size of the MT nuclei is generally as small as a few nanometers due to the presence of the tetragonal constrain of the cubic AUS lattice. In Fig. 4(b) of transient 2, the growth of the MT nuclei is evidently controlled by the crystallographic symmetry. It is known that growth of the MT nuclei is governed by phonon propagation and the distribution of strain fields in the crystals. In the case of $\text{Mn}_{50}\text{Ni}_{40}\text{Sn}_{10}$, we note that the growth of MT nuclei is constrained by the strain field followed by the C_4 symmetry, i.e., a fundamental symmetric element in the AUS phase. Therefore, we often observe a transient state in large crystalline samples with tweed structures, in which there is local atomic motion within twinning structures, as recognized

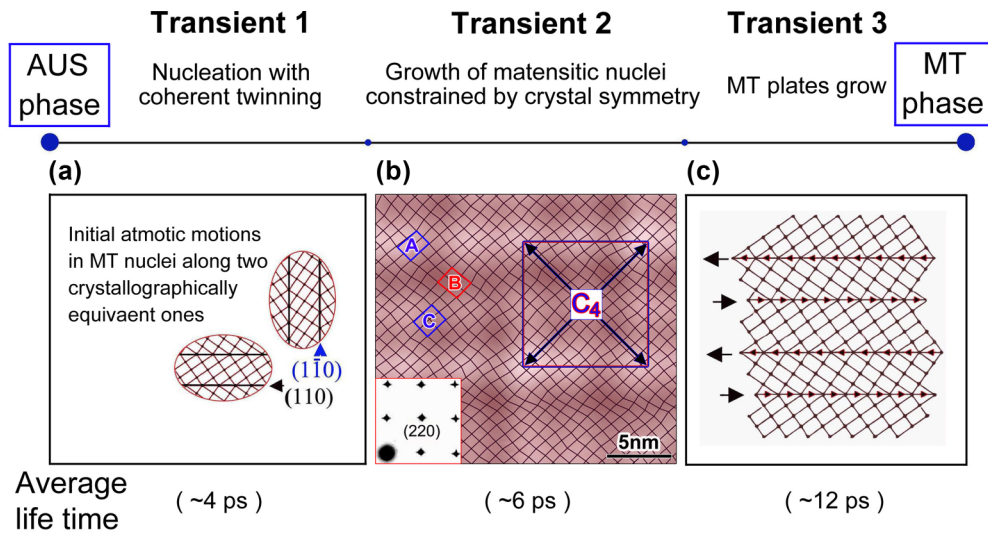


FIG. 4. Summary of the atomic motion and lattice dynamics for MT transition. (a) Transient 1: the martensitic nucleation with a coherent twinning nature. (b) Transient 2: the MT nuclei growth is constrained by lattice strain with the C_4 symmetry from the AUS phase. Local twinning relations and orthorhombic distortion can be clearly observed, such as in areas A , B , and C . This domain structure pattern is similar with the tweed structures as mentioned in Fig. 3, the bright areas clearly show orthorhombic transition, and the lattice distortion is schematically illustrated using the method reported in Ref. [35]. (c) Transient 3: the MT nuclei grow rapidly following the symmetry breaking, and the atomic movements in the MT plates go along the twinning planes, as indicated by arrows.

between area A and area B or between area B and area C in Fig. 4(b). Our measurements show that this transient state often has a lifetime of approximately 6 ps, and then the lattice thermalization and atomic motions overcome the constrain of the C_4 symmetry and drive the system toward the orthorhombic MT phase. In Fig. 4(c) of transient 3, after symmetry breaking of the crystal lattice the MT nuclei grow rapidly, and the atomic movements in the MT plates are parallel to the (110) twinning planes, as indicated by the arrows. The large MT plate phase is formed within 12 ps, which depends slightly on the crystal size and thickness.

In summary, we have reported a 4D-TEM study of the MT transition in a Heusler alloy $Mn_{50}Ni_{40}Sn_{10}$, where a variety of dynamic structural properties and transient states have been observed at picosecond time scales. The 4D-TEM images and diffraction observations clearly show that the MT transition and MT domain nucleation are associated with the collective atomic motion at picosecond time scales. Moreover, a strong coupling between the MT transition and lattice breathing mode is discovered in this system, which results in a periodic structural oscillation between the MT phase and the AUS phase. A careful analysis of the ultrafast

images and the corresponding electron diffraction patterns demonstrated the presence of the remarkable transient states, i.e., MT nucleation with a coherent twinning nature, the constraint of C_4 symmetry on the growth of the MT nuclei, and the rapid growth of MT plates. These results highlight the ability of 4D-TEM to directly probe the collective atomic motion related to symmetric breaking and to understand the mechanisms of domain/wall nucleation in multifunctional materials.

We thank Prof. Y. G. Shi and Prof. G. H. Wu for their support in sample preparations. This work was supported by the National Key Research and Development Program of China (Grant No. 2016YFA0300303), the National Basic Research Program of China 973 Program (Grants No. 2015CB921300 and No. 2012CB821404), the Natural Science Foundation of China (Grants No. 11604372, No. 11274368, No. 51272277, No. 91221102, No. 11190022, No. 11474323, and No. 91422303), and the ‘‘Strategic Priority Research Program (B)’’ of the Chinese Academy of Sciences (Grant No. XDB07020000).

M.Z. and G.C. contributed equally to this work.

- [1] P. J. Webster, *Contemp. Phys.* **10**, 559 (1969).
- [2] K. Ullakko, J. K. Huang, C. Kantner, R. C. OHandley, and V. V. Kokorin, *Appl. Phys. Lett.* **69**, 1966 (1996).
- [3] G. D. Liu *et al.*, *Solid State Commun.* **130**, 687 (2004).
- [4] H. F. Tian, J. B. Lu, L. Ma, H. L. Shi, H. X. Yang, G. H. Wu, and J. Q. Li, *J. Appl. Phys.* **112**, 033904 (2012).
- [5] L. Ma, S. Q. Wang, Y. Z. Li, C. M. Zhen, D. L. Hou, W. H. Wang, J. L. Chen, and G. H. Wu, *J. Appl. Phys.* **112**, 083902 (2012).
- [6] K. Oikawa, L. Wulff, T. Iijima, F. Gejima, T. Ohmori, A. Fujita, K. Fukamichi, R. Kainuma, and K. Ishida, *Appl. Phys. Lett.* **79**, 3290 (2001).
- [7] K. Bhattacharya and R. D. James, *J. Mech. Phys. Solids* **47**, 531 (1999).
- [8] T. Y. Hsu, *J. Phys. IV* **112**, 29 (2003).
- [9] B. J. Siwick, J. R. Dwyer, R. E. Jordan, and R. J. D. Miller, *Science* **302**, 1382 (2003).
- [10] C. I. Bлага, J. L. Xu, A. D. DiChiara, E. Sistrunk, K. K. Zhang, P. Agostini, T. A. Miller, L. F. DiMauro, and C. D. Lin, *Nature (London)* **483**, 194 (2012).
- [11] S. H. Nie, X. Wang, H. Park, R. Clinite, and J. M. Cao, *Phys. Rev. Lett.* **96**, 025901 (2006).

- [12] A. Cavalleri, C. Toth, C. W. Siders, J. A. Squier, F. Raksi, P. Forget, and J. C. Kieffer, *Phys. Rev. Lett.* **87**, 237401 (2001).
- [13] H. Ichikawa, S. Nozawa, T. Sato, A. Tomita, K. Ichiyangi, M. Chollet, L. Guerin, N. Dean, A. Cavalleri *et al.*, *Nat. Mater.* **10**, 101 (2011).
- [14] C. E. Graves, A. H. Reid, T. Wang, B. Wu, S. de Jong, K. Vahaplar, I. Radu, D. P. Bernstein, M. Messerschmidt, L. Mueller *et al.*, *Nat. Mater.* **12**, 293 (2013).
- [15] B. Barwick, H. S. Park, O. H. Kwon, J. S. Baskin, and A. H. Zewail, *Science* **322**, 1227 (2008).
- [16] A. Feist, K. E. Echternkamp, J. Schauss, S. V. Yalunin, S. Schafer, and C. Ropers, *Nature (London)* **521**, 200 (2015).
- [17] T. LaGrange, G. H. Campbell, B. Reed, M. Taheri, J. B. Pesavento, J. S. Kim, and N. D. Browning, *Ultramicroscopy* **108**, 1441 (2008).
- [18] F. Carbone, O. H. Kwon, and A. H. Zewail, *Science* **325**, 181 (2009).
- [19] G. L. Cao, S. S. Sun, Z. W. Li, H. F. Tian, H. X. Yang, and J. Q. Li, *Sci. Rep.* **5**, 8404 (2015).
- [20] D. J. Flannigan and A. H. Zewail, *Nano Lett.* **10**, 1892 (2010).
- [21] S. S. Sun, L. L. Wei, Z. W. Li, G. L. Cao, Y. Liu, W. J. Lu, Y. P. Sun, H. F. Tian, H. X. Yang, and J. Q. Li, *Phys. Rev. B* **92**, 224303 (2015).
- [22] N. Erasmus, M. Eichberger, K. Haupt, I. Boshoff, G. Kassier, R. Birmurske, H. Berger, J. Demsar, and H. Schwoerer, *Phys. Rev. Lett.* **109**, 167402 (2012).
- [23] D. J. Flannigan, B. Barwick, and A. H. Zewail, *Proc. Natl. Acad. Sci. USA* **107**, 9933 (2010).
- [24] H. N. Chapman, *Nat. Mater.* **8**, 299 (2009).
- [25] R. P. Chatelain, V. R. Morrison, B. L. M. Klarenaar, and B. J. Siwick, *Phys. Rev. Lett.* **113**, 235502 (2014).
- [26] C. Bungaro, K. M. Rabe, and A. Dal Corso, *Phys. Rev. B* **68**, 134104 (2003).
- [27] H. R. Zhang, C. Ma, H. F. Tian, G. H. Wu, and J. Q. Li, *Phys. Rev. B* **77**, 214106 (2008).
- [28] See Supplemental Material at <http://link.aps.org/supplemental/10.1103/PhysRevB.96.174203> for detailed descriptions of the schematic illustration of the ultrafast pump-probe experiment, sample preparation and structural characterization, the electron-energy-loss spectra, the Beer-Lambert law with the absorbed energy density, and the method for data processing.
- [29] H. E. Karaca, I. Karaman, B. Basaran, Y. J. Chumlyakov, and H. J. Maier, *Acta Mater.* **54**, 233 (2006).
- [30] Z. Lin, L. V. Zhigilei, and V. Celli, *Phys. Rev. B* **77**, 075133 (2008).
- [31] B. Rethfeld, A. Kaiser, M. Vicanek, and G. Simon, *Phys. Rev. B* **65**, 214303 (2002).
- [32] H. Park, X. Wang, S. Nie, R. Clinite, and J. Cao, *Phys. Rev. B* **72**, 100301 (2005).
- [33] S. O. Mariager, C. Dornes, J. A. Johnson, A. Ferrer, S. Gruebel, T. Huber, A. Caviezel, S. L. Johnson, T. Eichhorn *et al.*, *Phys. Rev. B* **90**, 161103 (2014).
- [34] T. Malis, S. C. Cheng, and R. F. Egerton, *J. Electron Microsc. Tech.* **8**, 193 (1988).
- [35] J. P. Sethna, S. Kartha, T. Castan, and J. A. Krumhansl, *Phys. Scr., T* **42**, 214 (1992).
- [36] C. Thomsen, J. Strait, Z. Vardeny, H. J. Maris, J. Tauc, and J. J. Hauser, *Phys. Rev. Lett.* **53**, 989 (1984).
- [37] D. R. Cremons, D. A. Plemmons, and D. J. Flannigan, *Nat. Commun.* **7**, 11230 (2016).